Materials Advances

PAPER

View Article Online
View Journal | View Issue

Cite this: *Mater. Adv.*, 2022, 3, 7348

Exploring the effect of partial B-site Al^{3+}–Mg^{2+} dual substitution on optoelectronic, surface, and photocatalytic properties of $BaTaO_2N$†

Mirabbos Hojamberdiev, *[ab] Ronald Vargas, [cd] Zukhra C. Kadirova,[ef] Katsuya Teshima [bg] and Martin Lerch[a]

$BaTaO_2N$ is appraised to be one of the few promising 600 nm-class photocatalysts for solar water splitting. However, the presence of structural defects and low charge separation limits its photocatalytic activity. Compared with mono substitution, dual substitution can be more effective in engineering the structural defects and improving the photocatalytic activity if foreign ions are suitably selected. In this work, we involve a dual-substitution approach to partially substitute Al^{3+} and/or Mg^{2+} for Ta^{5+} in $BaTaO_2N$. By maintaining the maximum concentration of Al^{3+}–Mg^{2+} dual substitution at 5%, the effect of the Al^{3+}–Mg^{2+} cosubstituent ratio on the optoelectronic, surface, and photocatalytic properties of $BaTaO_2N$ is investigated. The Al^{3+}–Mg^{2+} dual substitution leads to the shift of optical absorption edge toward shorter wavelengths, increasing the optical bandgap energy of $BaTaO_2N$. This effect is more pronounced in the samples with a higher concentration of Mg^{2+} due to the replacement of N^{3-} by a large number of O^{2-} to compensate charge balance. The initial reaction rates for the evolution of O_2 and H_2 reveal the improvement in the photocatalytic activity of $BaTaO_2N$ due to the partial Al^{3+}–Mg^{2+} dual substitution. Higher O_2 evolution is observed in the samples with a higher concentration of Mg^{2+}, while the H_2 evolution rate significantly relies on the increased concentration of Al^{3+}. According to the density functional theory (DFT) calculations, the effective masses of electrons become slightly lower than that of pristine $BaTaO_2N$ after partial Al^{3+}–Mg^{2+} (co)substitution, while a contrary tendency is observed for the effective masses of holes. The calculated positions of the valence band maximum and conduction band minimum are aligned with respect to the normal hydrogen electrode (NHE), and partial Al^{3+}–Mg^{2+} (co)substituted $BaTaO_2N$ photocatalysts can be promising candidates for visible-light-induced water splitting.

Received 30th May 2022,
Accepted 3rd August 2022

DOI: 10.1039/d2ma00611a

rsc.li/materials-advances

1. Introduction

As a carbon-free chemical process to generate green hydrogen, solar water splitting depends on various important photochemical and photophysical properties of photocatalytic materials. Particularly, band structure, optical absorption, charge density, charge mobility, charge separation, defect density, surface structure, particle size, crystallinity, *etc.* can be modulated by (co)substituting cations and anions in the crystal structures of host photocatalytic materials by foreign ions to improve their solar water-splitting efficiency.[1,2]

Many efforts have so far been made to enhance the water-splitting efficiency of various oxide and non-oxide photocatalytic materials by a cosubstitution. For instance, an apparent quantum yield (AQY) of 3.2% under visible light (420–800 nm) was reached by partial substitution of In^{3+} for Bi^{3+} and Mo^{6+} for V^{5+} in the host lattice of scheelite *m*-$BiVO_4$ due to uplifting the conduction band edge position above the proton reduction potential (0 V_{RHE} at

[a] *Institut für Chemie, Technische Universität Berlin, Straße des 17. Juni 135, 10623 Berlin, Germany. E-mail: khujamberdiev@tu-berlin.de, hmirabbos@gmail.com*
[b] *Department of Materials Chemistry, Shinshu University, Nagano 380-8553, Japan*
[c] *Instituto Tecnológico de Chascomús (INTECH) – Consejo Nacional de Investigaciones Científicas y Técnicas (CONICET)/Universidad Nacional de San Martín (UNSAM), Avenida Intendente Marino, Km 8,2, (B7130IWA), Chascomús, Provincia de Buenos Aires, Argentina*
[d] *Escuela de Bio y Nanotecnologías, Universidad Nacional de San Martín (UNSAM), Avenida Intendente Marino, Km 8,2, (B7130IWA), Chascomús, Provincia de Buenos Aires, Argentina*
[e] *Department of Inorganic Chemistry, National University of Uzbekistan, 100174 Tashkent, Uzbekistan*
[f] *Uzbekistan-Japan Innovation Center of Youth, University Street 2B, 100095 Tashkent, Uzbekistan*
[g] *Research Initiative for Supra-Materials, Shinshu University, 4-17-1 Wakasato, Nagano 380-8553, Japan*

† Electronic supplementary information (ESI) available. See DOI: **https://doi.org/10.1039/d2ma00611a**

pH = 7).[3] Compared with pristine $BiVO_4$, 0.5W–2Mo–$BiVO_4$ exhibited a significant increase in the donor concentration (N_D = 1.03×10^{28} m^{-3}), lifetime (τ_D = 3.8 s), and incident photon conversion efficiency (IPCE = 41%), a decrease in the flat band potential (V_{fb} = 0.35 V_{RHE}) and space charge layer thickness, and nearly ten times higher H_2 evolution.[4] A photocurrent density of 1.97 mA cm^{-2} at 1.23 V_{RHE} and a relatively low onset potential of 0.68 V_{RHE} were obtained by a simultaneous introduction of Sn and Mo in α-Fe_2O_3, where the former accelerated charge separation by improving conductivity and the latter induced high density of surface trapping states, leading to the inhibition of charge recombination kinetics in surface states.[5] A significant increase in the concentration of (co)doped ions decreases the efficiency. By applying a computational method, Smart *et al.*[6] recently found a doping clustering, which traps free-electron polarons and severely lowers the carrier concentration with respect to the doping concentration, to be responsible for the doping bottleneck in α-Fe_2O_3, and proposed a codoping with dopants having low binding energies for clustering, such as Sn–Ti, as a solution. The formation of oxygen vacancies in $SrTiO_3$, which act as electron–hole recombination centers, was suppressed by Rh–La[7] and La–Al[8] codoping, resulting in apparent quantum yields of 1.1% at 420 nm and 78.43% under 365 nm, respectively. Layered perovskite Sr_2TiO_4 was activated by La/N codoping, using 0.5 wt% Rh/Cr_2O_3 as a cocatalyst, for overall water splitting under visible light due to the contribution of N and La for uplifting the valence band edge position and charge balancing, respectively.[9] Wide-band-gap photocatalysts, such as $NaTaO_3$,[10] $BaTa_2O_6$,[11] and $KTaO_3$,[12] were activated for H_2 evolution under visible light irradiation by introducing the Ir/La codopants. Along with La as a charge balancer, doped Ir could form relatively shallow impurity levels, and the H_2 evolution could proceed by electron transition from the impurity levels formed by Ir^{3+} to the conduction band. A negative shift in the onset potential of photoelectrochemical water splitting from about 0.8 V_{RHE} (for pristine Ta_3N_5) to 0.55 V_{RHE} under AM 1.5 G-simulated sunlight was observed for a Mg–Zr cosubstituted Ta_3N_5 photoanode because of the change in the bandgap potential.[13] Very recently, Mg–Zr-codoped single-crystalline Ta_3N_5 exhibited 45-times greater photocatalytic water-reduction activity than undoped Ta_3N_5 and an outstanding apparent quantum yield (AQY) of 0.54% at 420 nm during the photocatalytic H_2 evolution reaction due to the simultaneously well-regulated defect species and surface properties.[14]

As a promising candidate for visible-light-driven water splitting because of its excellent visible light absorption up to 660 nm, narrow band gap, sufficient valence band potential for water oxidation, good stability, and nontoxicity,[15] perovskite $BaTaO_2N$ has gained significant research interest. Apparent quantum yields (AQY) of 0.06%,[16] 2.1%,[17] 6.8%,[18] and 11.9%[19] at 420 nm were progressively achieved for photocatalytic H_2 and O_2 evolution over $BaTaO_2N$, respectively, and an incident photon-to-current efficiency of ≈43% at 1.23 V_{RHE} was obtained in photoelectrochemical water oxidation over $BaTaO_2N$.[20] In addition to other important strategies applied, such as flux growth,[21] particle morphology- and size-controlled synthesis,[22] time-retrenched synthesis,[23] thin-film fabrication,[24] facet-controlled synthesis,[25,26] solid–solution,[16,27] surface modification,[19] tensile uniaxial strain,[28] and particle transfer method,[29] the *A*-site or *B*-site substitution or partial substitution of atoms with different radii or valences have been proven to be effective in tailoring the surface local structure and anion ordering and modulating the optical, electronic, surface, and photocatalytic properties of $BaTaO_2N$ without altering its perovskite structure. Substituents with different valences act as either electron donors or acceptors and change the carrier concentration when introduced into the host lattice.[30] Although divalent (Mg^{2+}, Ca^{2+}, Sr^{2+}, and Zn^{2+}), trivalent (Al^{3+}, Ga^{3+}, and Sc^{3+}), tetravalent (Ti^{4+} and Zr^{4+}), and hexavalent (Mo^{6+} and W^{6+}) cations were singly introduced into the $BaTaO_2N$ lattice to improve its photocatalytic and photoelectrochemical water splitting efficiency,[17,28,31–35] a dual-substitution effect on water splitting efficiency of $BaTaO_2N$ has not been explored yet.

Many outstanding works, including the above-mentioned ones, on the enhancement of water splitting efficiency of various photocatalytic materials by a dual substitution and our recent work,[32] where 5% Mg^{2+} and 5% Al^{3+} independently promoted the photocatalytic sacrificial O_2 and H_2 evolution over $BaTaO_2N$ under visible light, respectively, inspired us to further explore the impact of a partial dual substitution on water splitting efficiency of $BaTaO_2N$. In this study, by maintaining the maximum concentration of partial Al^{3+}–Mg^{2+} dual substitution at 5%, the effect of the Al^{3+}–Mg^{2+} cosubstituent ratio on the optoelectronic, surface, and photocatalytic properties of $BaTaO_2N$ is studied. By linking the materials characterization results to the evaluated photocatalytic activity, the contribution of the partial Al^{3+}–Mg^{2+} dual substitution is discussed and insights into the possible underlying mechanisms are gained.

2. Experimental

2.1. Synthesis

Pristine and Al^{3+}–Mg^{2+} cosubstituted $BaTaO_2N$ powders were synthesized by a solid-state reaction route. $BaCO_3$ (99.99%, chemPUR), Ta_2O_5 (99%, Alfa Aeser), and Al_2O_3 (99.99%, Merck) or $MgCO_3$ (>99%, Merck) as cosubstituent sources were first mixed manually in a stoichiometric ratio. Then, the well-homogenized mixture was placed in a platinum crucible, heated at 950 °C for 6 h using a localized NH_3 delivery system (12.5 L h^{-1}), with a heating rate of 500 °C h^{-1} and a natural cooling rate. The synthesized $BaTaO_2N$ (BTON) powders: with no substituent, 5% Al^{3+}, 5% Mg^{2+}, 2.5% Al^{3+} + 2.5% Mg^{2+}, 3.5% Al^{3+} + 1.5% Mg^{2+}, and 1.5% Al^{3+} + 3.5% Mg^{2+} were labeled as BTON1, BTON2, BTON3, BTON4, BTON5, and BTON6, respectively.

2.2. Characterization

The crystal structure was determined by X-ray diffraction (XRD; PANalytical X'Pert PRO) analysis using Cu-K_α radiation (Bragg–Brentano geometry). The microstructure was examined by scanning electron microscopy (SEM; GeminiSEM 500 NanoVP, Carl Zeiss). The elemental content was analyzed by means of energy-dispersive X-ray spectroscopy (EDX; DSM 982 GEMINI, Carl Zeiss, with a Bruker Quantax XFlash® 6|60) and inductively coupled plasma-optical emission spectrometry (SPS5510, SII Nanotechnology Inc.). The UV-Vis diffuse reflectance spectra were measured using an Evolution 220 UV/Vis spectrometer (Thermo Fisher Scientific). The surface chemical composition and states of elements were analyzed using a PHI Quantera II scanning X-ray photoelectron microprobe (XPS; ULVAC-PHI, Inc.) with monochromatic Al-K_{α} radiation. The XPS profiles were fitted using a Gaussian–Lorentzian function, and the peak positions were normalized by positioning the C 1s peak at 284.5 eV.

2.3. Photocatalytic activity tests

The photocatalytic activity of pristine and (co)substituted $BaTaO_2N$ samples was evaluated by comparing their H_2 and O_2 evolution promoted by Pt (0.5 wt%) and CoO_x (2 wt% Co) cocatalysts, respectively. The cocatalysts were loaded according to the processes reported elsewhere.[32] The H_2 and O_2 evolution half-reactions were separately carried out in a Pyrex® side-irradiation-type reactor connected to a closed gas circulation and evacuation system. A 300 W Xe arc lamp (Cermax-PE300BF, PerkinElmer) with a UV-cutoff filter (L42, HOYA) and a cold mirror (CM-1, Optline) was used as the visible-light source, and the irradiance of visible light was 200 mW cm^{-2}. The quantity of evolved gases was analyzed by using a gas chromatograph (GC-8A, TCD, Ar gas carrier, Shimadzu), which was directly connected to the reactor. For the O_2-evolution half-reaction, 100 mg of CoO_x-loaded photocatalyst, 300 mL of 10 mM $AgNO_3$ (sacrificial electron scavenger), and 200 mg of La_2O_3 (pH buffer) were used, while 100 mg of Pt-loaded photocatalyst and 300 mL of 10 vol% aqueous methanol solution were used for the H_2-evolution half-reaction.

2.4. Computational methods

Density functional theory (DFT) simulations were performed within *Vienna ab initio simulation package* (VASP)[36,37] in the projector augmented waves (PAW) scheme. The pristine $BaTaO_2N$ cell ($Pm\bar{3}m$ space group, No. 221, $Z = 1$) was created based on the experimental structural data.[38] Several types of substitution have been considered in the present work. A 2 × 1 × 1 supercell was used to simulate a 50 at% substitution content of Al or Mg, *i.e.*, one substituent atom was substituted for Ta atom within the 10-atomic supercell. To model the cosubstitution contents of 25 at% Al and 25 at%. Mg, one Al and one Mg atom were substituted for two Ta atoms within the 20-atomic 2 × 2 × 1 supercell. Simulation of 50 at% substitution, where one quarter is Al and three quarters is Mg, and *vice versa* were modeled within a 2 × 2 × 2 supercell with 40 atoms. All simulated configurations with the corresponding chemical compositions are listed in Table S1 (ESI†). The generalized gradient approximation (GGA) of the exchange-correlation potential in the PBE form[39] was adopted during geometry optimization. For the 2 × 1 × 1 and 2 × 2 × 1 supercells, Γ-centered 6 × 12 × 12 and 6 × 12 × 12 *k*-point grids were used, respectively. In the case of the 2 × 2 × 2 supercell, the Monkhorst–Pack *k*-point mesh 6 × 6 × 6 was applied.[32] The cut-off energy was 400 eV for all models. The optimization continued until the residual forces on the atoms became less than 0.5 meV $Å^{-1}$. The totally relaxed pristine and (co)substituted models were adopted for further calculations of the density of states (DOS) and band structures. To achieve the best agreement between experimental and theoretical results, the screened Coulomb hybrid HSE12s exchange–correlation functional was employed.[40] During the calculation of the DOS structure, Γ-centered 6 × 12 × 12, 4 × 4 × 8, and 3 × 3 × 3 *k*-point grids in the case of (co)substituted models within the 2 × 1 × 1, 2 × 2 × 1, and 2 × 2 × 2 supercells were applied, respectively. The Gaussian smearing method was used for the electronic structure calculations. The effective masses of electrons and holes were calculated using the Sumo-bandstats program through the parabolic fitting to the conduction band minimum (CBM) and valence band maximum (VBM).[41] The band edge positions were calculated according to the empirical formula:[42–45]

$$E_{CB} = \chi - E^{e} - 0.5\, E_{g} \quad (1)$$

$$E_{VB} = E_{CB} - E_{g} \quad (2)$$

where E_{CB} and E_{VB} are the CB and VB edge potentials, respectively, E_g is the band gap. The Mulliken electronegativity of semiconductor χ can be calculated as the geometric mean of the absolute electronegativities of the constituent atoms. This is defined as the arithmetic mean of the electron affinities and atomic ionization. E^e is the energy of free electrons of the hydrogen scale (4.5 eV).[46,47]

3. Results and discussion

Since doping can also influence the formation of a secondary phase depending on its concentration,[48] the crystal structure and purity of the synthesized samples were first analyzed by X-ray powder diffraction (XRD) analysis. The XRD patterns of pristine and (co)substituted samples are shown in Fig. 1. All reflections in the XRD patterns are identified as a single-phase cubic perovskite $BaTaO_2N$ with the space group $Pm\bar{3}m$ (ICDD PDF 01-084-1748), and no reflections assignable to impurity phases are detected. In the perovskite structure of $BaTaO_2N$, Ba cations with a larger ionic radius occupy *A* site and has a 12-fold coordination, while Ta cations with a smaller ionic radius occupy a *B* site and have a 6-fold coordination at the octahedral sites. Since the ionic radii of Al^{3+} (53.5 pm) and Mg^{2+} (72 pm) substituents are closer to that of Ta^{5+} (64 pm) than that of Ba^{2+} (161 pm), both are expected to be (co)substituted for Ta^{5+}. Apparently, the magnified XRD patterns indicate a slight alteration in the 2θ angle position of the 110 reflection toward higher or lower 2θ angles when Ta^{5+} is partially substituted by Al^{3+} (BTON2) or Mg^{2+} (BTON3) in the octahedral coordination, indicating the lattice volume contraction or expansion, respectively.[32] As the ionic radius of Al^{3+} is smaller than that of Ta^{5+}, while the ionic radius of Mg^{2+} is larger than that of Ta^{5+}, the 2θ angle position of the 110 reflections of the Al^{3+}–

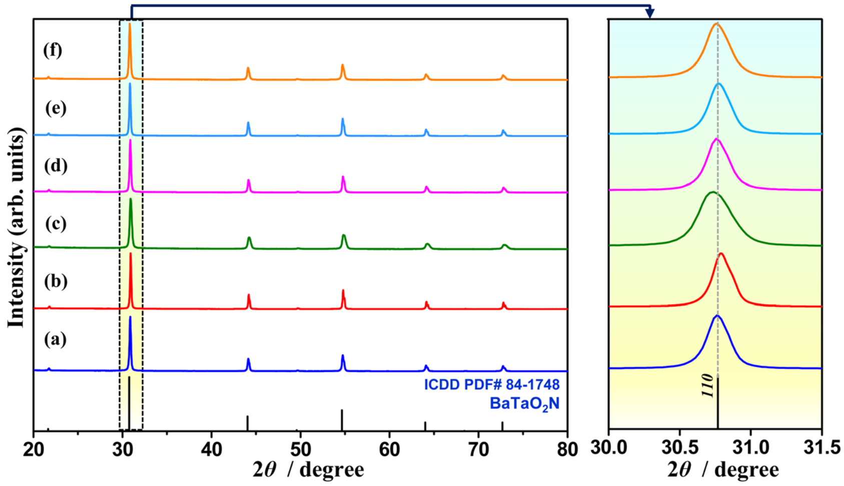

Fig. 1 X-Ray diffraction patterns of BTON1 (a), BTON2 (b), BTON3 (c), BTON4 (d), BTON5 (e), and BTON6 (f).

Mg^{2+} dual-substituted samples (BTON4-6) is near to that of pristine $BaTaO_2N$ (BTON1). Also, the concurrent substitution of smaller O^{2-} (126 pm) for larger N^{3-} (157 pm) to compensate charge balance in the Al^{3+}–Mg^{2+} dual-substitution for Ta^{5+} may have lessened the lattice expansion.[13,32] An opposite trend was observed when oxygen occupying the substitutional and interstitial lattice sites of $K_2La_2Ti_3O_{10}$ was intentionally substituted by nitrogen.[49] As the (co)substitution concentration is strictly controlled at 5%, no significant distortion in the crystal structure of $BaTaO_2N$ is observed.

The photocatalytic water splitting activity of photocatalysts is greatly influenced by particle morphology, size, porosity, exposed facets, *etc.* Recently, it was found that the CoO_x cocatalyst could function more effectively in photoluminescence quenching and generating greater band bending on the {010} facet in dual-faceted $BiVO_4$ with respect to the {110} facet.[50] Also, the $BaTaO_2N$ crystals with well-developed {111} facets[25] and coexposed anisotropic {100} and {110} facets[26] showed a significantly enhanced photocatalytic activity for H_2 evolution in comparison to the $BaTaO_2N$ crystals with only {100} facets. Thus, the microstructures of pristine and (co)substituted samples were also analyzed, and the SEM images are shown in Fig. 2. Pristine $BaTaO_2N$ (BTON1) has irregular particles with an average size of 247 nm, and some particles contain pores (Fig. 2a). Evidently, the particle morphology and size were affected by changing the Al^{3+}–Mg^{2+} cosubstituent ratio. Namely, introducing 5% Al^{3+} (BTON2) significantly reduced the number of small particles, and large bulky particles with an average size of 338 nm and surface pores were formed (Fig. 2b). On one hand, these surface pores can, in principle, provide a large surface area that is beneficial for the photocatalytic water splitting reactions and also a greater number of dangling bonds that can act as nucleation centers for cocatalyst particles.[22] On the other hand, they can also affect both charge transport within the photocatalyst and mass transfer of reactants and products, impacting the overall reaction kinetics.[51] In Fig. 2c, the particle size was drastically decreased to an average size of 87 nm, and the particles became more joined with an intimate contact and without any surface pores after substituting 5% Mg^{2+} for Ta^{5+} (BTON3). When 2.5%

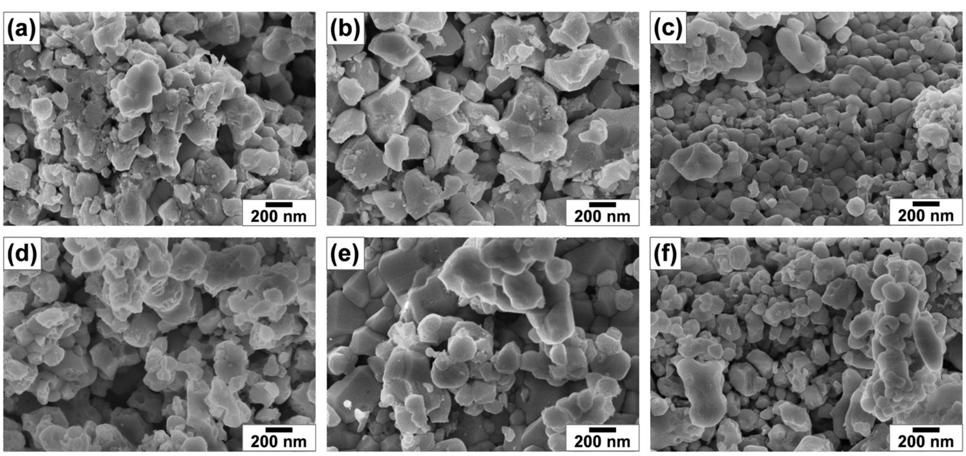

Fig. 2 SEM images of BTON1 (a), BTON2 (b), BTON3 (c), BTON4 (d), BTON5 (e), and BTON6 (f).

Al^{3+} and 2.5% Mg^{2+} (BTON4) were equally cosubstituted for Ta^{5+} (BTON4), the particles again became larger (285 nm) without a clear outline (Fig. 2d). When the Al^{3+} : Mg^{2+} cosubstituent ratio was set to 3.5% : 1.5% (BTON5), larger and denser crystals with idiomorphic shapes appeared along with smaller irregular particles with surface pores (Fig. 2e). In contrast, when the Al^{3+} : Mg^{2+} cosubstituent ratio was adjusted to 1.5% : 3.5% (BTON6), the average particle size was reduced to 93 nm (Fig. 2f). This indicates that the total interfacial free energy and kinetic factors were more substantially influenced by Mg^{2+} than Al^{3+}. In the previous study,[32] the partial substitution of Mg^{2+} for Ta^{5+} in $BaTaO_2N$ similarly reduced the number of plate-like particles and led to the formation of particles with idiomorphic shapes in comparison to other substituents. Furthermore, the solid-state reaction here induced the formation of more irregular particles despite Al^{3+}–Mg^{2+} dual substitution in comparison to the flux method applied previously to synthesize $BaTaO_2N$ particles,[23,32,52] which may lead to the different photocatalytic activity. The EDX spectra of pristine and (co)substituted samples shown in Fig. S1 (ESI†) reveal the presence of Ba, Ta, O, N, Al, and Mg elements. The (co)substituent contents estimated by EDX and ICP-OES data are about 4.84% Al, 4.91% Mg, 2.42% Al + 2.38% Mg, 3.47% Al + 1.52% Mg, and 1.48% Al + 3.51% Mg for BTON2, BTON3, BTON4, BTON5, and BTON6, respectively, which are close to the nominal compositions of (co)substituents.

Fig. 3 shows the UV-Vis diffuse reflectance spectra of pristine and (co)substituted samples. Pristine $BaTaO_2N$ (BTON1) has an optical absorption edge at 665 nm, corresponding to the optical bandgap energy of 1.86 eV. Obviously, the Al^{3+}–Mg^{2+} cosubstituent ratio influenced visible-light absorption of $BaTaO_2N$. That is, the optical absorption edges of (co)substituted samples shifted toward shorter wavelengths, resulting in the optical bandgap energies of 1.90, 2.01, 1.96, 1.93, and 1.99 eV for BTON2, BTON3, BTON4, BTON5, and BTON6, respectively. Interestingly, increasing the concentration of Mg^{2+} led to a greater shift toward shorter wavelengths in comparison to that of Al^{3+}. This is due to the substitution of more N^{3-} by O^{2-} to compensate charge balance in the Mg^{2+}-to-Ta^{5+} substitution.[13,32,34] The valence band of $BaTaO_2N$ consists of hybridized N 2p and O 2p orbitals, and its position is affected by the N/O ratio as the N 2p orbitals are higher in energy than the O 2p orbitals. This is also reflected by the powder color of the synthesized samples shown in the insets of Fig. 3, where the higher the Mg^{2+} concentration, the brighter the powder color is. Although the Al^{3+}–Mg^{2+} dual substitution induced a considerable blue-shift in light absorption, which is not beneficial in solar energy conversion, it is still advantageous in reducing the surface and bulk defects because of the suppression of Ta^{5+} reduction by Al^{3+}/Mg^{2+} (co)substitution and altering the band edge positions with respect to water splitting potentials.[53]

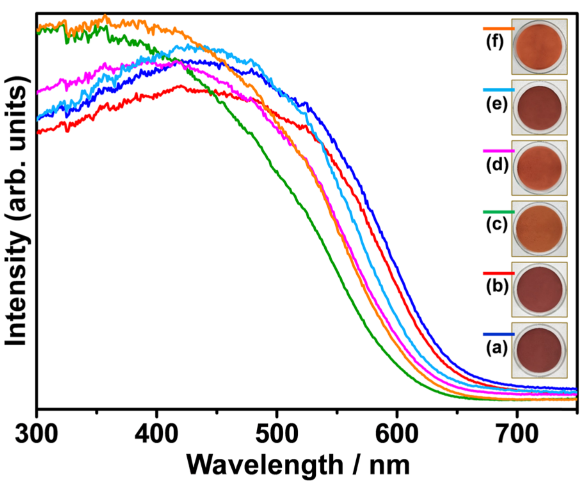

Fig. 3 UV-Vis diffuse reflectance spectra of BTON1 (a), BTON2 (b), BTON3 (c), BTON4 (d), BTON5 (e), and BTON6 (f).

To probe the surface chemical composition and oxidation state of elements, X-ray photoelectron spectroscopy (XPS) measurements were conducted. In the XPS core-level spectra of Ta 4f in Fig. 4, the overlapping peaks of the Ta $4f_{5/2}$ and Ta $4f_{7/2}$ states of the Ta^{5+} species bonded to N^{3-} and O^{2-} can be deconvoluted into four different peaks centered at the binding energies of 25.70–26.16, 23.67–24.14, 27.07–27.11, and 25.01–26.09 eV, respectively.[54] Although there is no direct correlation between the intensities of the Ta(N) and Ta(O) peaks and Al^{3+}–Mg^{2+} (co)substitution ratio, a slightly higher intensity in the Ta(O) peak can be observed in comparison to that of the Ta(N) peak when the Al^{3+} : Mg^{2+} (co)substituent ratio is decreased because a large number of N^{3-} were substituted by O^{2-} to compensate charge balance in the Mg^{2+}-to-Ta^{5+} substitution.[13,32,34] No peaks associated with reduced tantalum species were noted as the partial substitution of Al^{3+} or/and Mg^{2+} suppressed the reduction of Ta^{5+}.[53] This leads to the reduction in the surface and bulk defects that can improve charge separation and photocatalytic activity.

Density functional theory (DFT) simulations were further involved to understand the electronic structures of pristine and (co)substituted $BaTaO_2N$ models. First, the structural parameters of pristine and (co)substituted $BaTaO_2N$ models were predicted by DFT-PBE. As shown in Table S1 (ESI†), the structural parameters of pristine $BaTaO_2N$ model were found to be in good agreement with the experimental data reported previously.[32,40] It can be noted that Al substitution leads to a contraction of lattice constants due to a smaller ionic radius of Al^{3+} (53.5 pm) than that of Ta^{5+} (64 pm). An opposite trend is observed in Mg substitution because the ionic radius of Mg^{2+} (72 pm) is larger than that of Ta^{5+}. The cosubstituted models can be characterized in the same manner depending on the Al and Mg contents. This is consistent with the X-ray diffraction data presented earlier.

Next, the effect of Al^{3+}–Mg^{2+} (co)substitution at the Ta site in $BaTaO_2N$ on electronic band structures was studied by DFT-HSE12s. As shown in Fig. 5, the estimated bandgap energy of pristine $BaTaO_2N$ is 1.49 eV (direct-type), which is slightly lower than the experimentally[32,55] and theoretically[56] obtained bandgap values due to the well-known underestimation. The calculation results reveal that the (co)substitution of Al and/or Mg at the Ta site in $BaTaO_2N$ can generate acceptor states above the valence band maximum, shifting the valence band upward (Fig. 5).

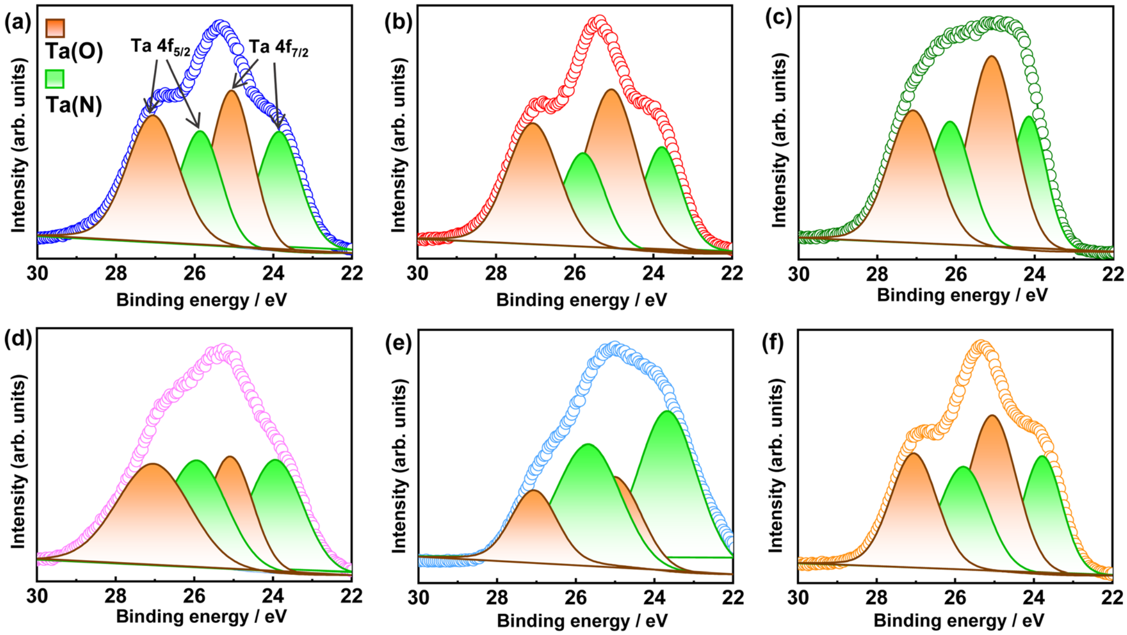

Fig. 4 Ta 4f high-resolution X-ray photoelectron spectra of BTON1 (a), BTON2 (b), BTON3 (c), BTON4 (d), BTON5 (e), and BTON6 (f).

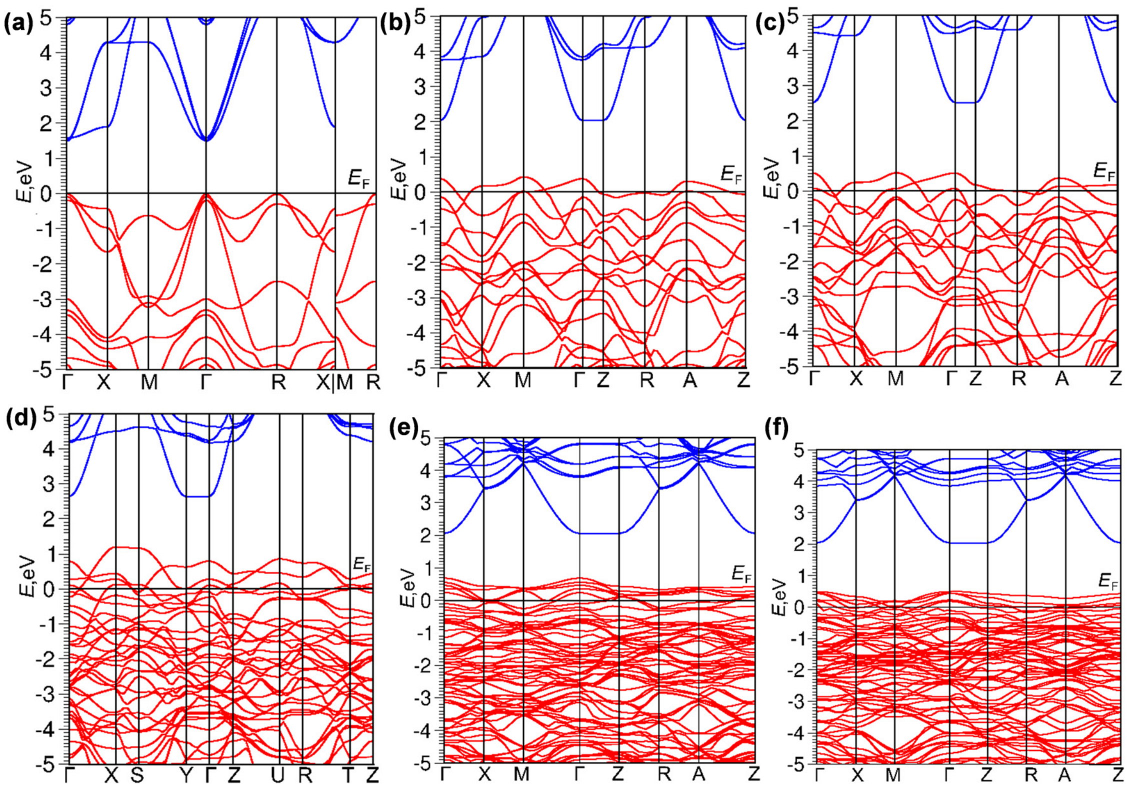

Fig. 5 Electronic band structures of (a) BTON,[32] (b) BTON : Al (50 at%), (c) BTON : Mg (50 at%), (d) BTON : Al : Mg (25 : 25 at%), (e) BTON : Al : Mg (37.5 : 12.5 at%), and (f) BTON : Al : Mg (12.5 : 37.5 at%). The Fermi level is set at 0 eV.

According to the density of states (DOS) plots, the distribution patterns of the atomic orbitals seem to be unchanged (Fig. S2, ESI†). The major contribution to the valence band comes from occupied O p and N p states, while the conduction band consists of empty Ta d states. The dependence of the bandgap value on Al or/and Mg contents in pristine and (co)substituted $BaTaO_2N$ models is shown in Fig. S3 (ESI†). Apparently, Al substitution results in a narrower bandgap value in comparison to Mg substitution. Meantime, three cosubstituted models are characterized by a significant decrease in the band gap with an increase in the Al content, which is beneficial to absorb a significant fraction of visible light. Among the three cosubstituted models, the $BaTa_{0.5}Al_{0.375}Mg_{0.125}O_2N$ model has the narrowest band gap (1.36 eV).

The effective masses of electrons (m_e^*) and holes (m_h^*) were also estimated along specific directions (Table S2, ESI†). It is known that lower effective masses of charge carriers indicate their higher mobility, which is important for enhancing the photocatalytic activity.[45] In the case of pristine $BaTaO_2N$, the effective masses of electrons and holes are comparable and low. With Al and/or Mg (co)substitution, the effective masses of electrons become slightly lower than that in pristine $BaTaO_2N$, suggesting an improvement in the reduction ability of the (co)substituted $BaTaO_2N$ models. A contrary tendency can be observed for the effective masses of holes, which increased three or more times as compared with that of pristine $BaTaO_2N$. The lowest effective masses of holes are noted for the $BaTa_{0.5}Al_{0.375}Mg_{0.125}O_2N$ model, which may exhibit its stronger oxidizing ability among (co)substituted compounds. Suitable redox potentials are also known as one of the major criteria for developing high-efficiency visible-light-active photocatalysts.[45,46] As shown in Table S3 (ESI†), the calculated positions of the valence band maximum and conduction band minimum are aligned with respect to the normal hydrogen electrode (NHE), and Al^{3+}–Mg^{2+} (co)substituted $BaTaO_2N$ photocatalysts can be promising candidates for visible-light-induced water splitting.

The effect of Al^{3+}–Mg^{2+} dual substitution on visible-light-induced photocatalytic activity of $BaTaO_2N$ was investigated. The half-reaction time courses for the photocatalytic H_2 and O_2 evolution over pristine and (co)substituted $BaTaO_2N$ samples are shown in Fig. 6. As shown in Fig. 6a, the quantity of evolved O_2 gradually increases in the following order within 5 hours of the photocatalytic reaction: 124.05 μmol < 171.4 μmol < 238.2 μmol < 271.5 μmol < 324.7 μmol < 406.2 μmol for BTON1, BTON2, BTON3, BTON5, BTON4, and BTON6, respectively. Clearly, compared with pristine $BaTaO_2N$ (BTON1) and mono-substituted samples (BTON2 and BTON3), cosubstituted samples exhibit higher O_2 evolution, and the highest O_2 evolution (406.2 μmol) is observed for BTON6 with 1.5% Al^{3+} + 3.5% Mg^{2+} cosubstituents. It is argued that due to the decrement in the surface and bulk defects as a result of the partial replacement of Ta^{5+} by a higher number of Mg^{2+} in the Al^{3+}–Mg^{2+} dual substitution and altering the valence band position with respect to water oxidation potential. As shown in Fig. 6b, the highest quantity of evolved H_2 is obtained for BTON5 (75.4 μmol) followed by BTON4 (60.5 μmol), BTON6 (51.9 μmol), BTON2 (45.4 μmol), BTON3 (31.7 μmol), and BTON1 (17.3 μmol), respectively.

Kisch and Bahnemann[57] suggested that the comparison of photocatalyst performance must be done using the kinetic parameters extracted from experimental measurements performed using the same types of light source and reactor. Then, it is convenient to estimate the reaction rate in the initial stages as the respective slope of the O_2 and H_2 evolved *vs.* irradiation time plots. For the O_2 evolution, the reaction rates were estimated to be 178.66, 102.64, 79.33, 66.65, 55.89, and 31.44 μmol h^{-1} for BTON6, BTON4, BTON5, BTON3, BTON2, and BTON1, respectively. For the H_2 evolution, 18.94, 12.81, 8.34, 7.35, 3.93, and 1.78 μmol h^{-1} for BTON5, BTON4, BTON6, BTON2, BTON3, and BTON1, respectively. Clearly, $BaTaO_2N$ modified with 1.48% Al + 3.51% Mg generated the highest quantity of O_2 (178.66 μmol h^{-1}) with an apparent quantum yield of 0.18% at 420 nm, and $BaTaO_2N$ modified with 3.47% Al + 1.52% Mg produced the highest quantity of H_2 (18.94 μmol h^{-1}) with an apparent quantum yield of 0.64% at 420 nm. Considering that the variation of the specific surface area between the photocatalysts does not have a greater impact,[58] the trend observed in the initial reaction rate can be considered as evidence that reflects the improvement of the surface reactions due to the modification of the $BaTaO_2N$ photocatalyst with Al^{3+}–Mg^{2+} dual substitution. In our recent work,[32] the photocatalytic reaction rate of the cation-modified $BaTaO_2N$ was correlated with the energy difference of the adsorbed intermediates, where the photocatalytic evolution of H_2 and O_2 was significantly enhanced using Al- and Mg-modified $BaTaO_2N$ photocatalysts, respectively. Thus, it is argued that in the case of dual substitution of $BaTaO_2N$ with

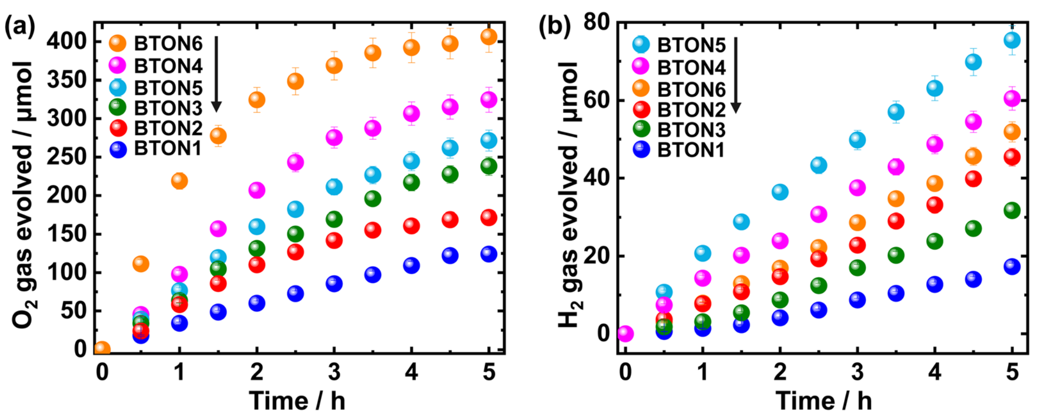

Fig. 6 Reaction time courses for photocatalytic O_2 (a) and H_2 (b) evolution over BTON1, BTON2, BTON3, BTON4, BTON5, and BTON6 loaded with CoO_x and Pt nanoparticles as O_2 and H_2 evolution cocatalysts under visible light irradiation.

Al^{3+} and Mg^{2+}, the photocatalytic performance to form H_2 can be favored in the photocatalyst with a higher proportion of Al^{3+}. Regarding the evolution of O_2, it was reported that the modification with Mg^{2+} presented a higher reaction rate than the undoped BTON and the Al-doped BTON.[32] The latter suggests that the highest reactivity for the evolution of O_2 can be achieved with the photocatalyst having the highest percentage of Mg^{2+}. Therefore, the Al^{3+}–Mg^{2+} dual substitution can modulate the photocatalytic activity of $BaTaO_2N$.

The Al^{3+}–Mg^{2+} dual substitution in $BaTaO_2N$ leads to the improvement in the kinetics of photocatalytic processes as a result of efficient electron transfer and the reduction of recombination processes. The interrelation of both phenomena (electron transfer and recombination) in $BaTaO_2N$ photocatalysts has been discussed in previous works,[13,20,23] and the optoelectronic properties were presented to be responsible for the changes in the photocatalytic behavior. For instance, the codoping of Ta_3N_5 with Mg and Zr[13] and the modification of $BaTaO_2N$ with Ca and cobalt oxide[17] significantly affected the optoelectronic properties in such a way that the co-doped photocatalysts could exhibit the lower onset potentials and higher photocatalytic activity for photoelectrochemical water splitting. Modification of $BaTaO_2N$ and $LaTiO_2N$ with Zn and Ca has also been shown to significantly influence carrier density, to shift the band edge position, and to improve the yield of photo-redox reactions.[33] Similar results have been reported in $BaTaO_2N$ with various dopants.[31,34]

For Al^{3+}–Mg^{2+}-(co)substituted $BaTaO_2N$, the photocatalytic performance observed for the evolution of O_2 and H_2 (Fig. 6), the changes in visible light absorption (Fig. 3), and DFT calculations (Fig. 5) support the alteration in the electronic states of the photocatalyst with Al^{3+} and/or Mg^{2+}. Therefore, the difference in the dynamics of charge carriers affected the photocatalytic performance of pristine and (co)substituted photocatalysts. The relevance of DFT calculations to detect band structure effects that correlate with photocatalytic activity is convenient. Using the DFT calculations, Ni *et al.*[59] estimated the changes in the electronic structure of ZnSe by co-substitution of Sb at Se sites and Sc or Y at Zn sites, suggesting the importance of the effect of strong Coulombic interactions. It was also noted that the dual substitution resulted in a reduced bandgap, absorption in visible light, and energetic position of the bands relative to the redox potentials of water. By applying the DFT calculations, the role of F and N in the co-doped TiO_2 was studied,[60] indicating that the co-substitution of foreign atoms affects the band structure and provides new pathways for the appearance of different physicochemical processes (*e.g.*, enhanced adsorption of reagents, formation of new bonds, changes in the band structure, *etc.*) that provide improvements to the photocatalytic activity. As the dynamics of charge carriers is defined by the electronic structure, the DFT results presented here for $BaTaO_2N$ cosubstituted with Al^{3+} and Mg^{2+} (Fig. 5) allow to assertively detect those changes in the electronic band structure that could have effects and/or be related to the performance of the photocatalysts. Further, the effect of Al^{3+}–Mg^{2+} dual substitution on surface property (water and methanol adsorption) of $BaTaO_2N$ is also theoretically explored.

Along with other factors, the adsorption of water molecules and formed intermediates on the photocatalyst surface has a strong influence on photocatalytic activity. In our recent work, the experimental photocatalytic reaction rates of pristine and cation-doped $BaTaO_2N$ surfaces terminated with TaO_6, TaN_6, and TaO_4N_2 were well presented using the adsorption energies of intermediates (H* for H_2 evolution and HO* and O* for O_2 evolution) estimated by molecular dynamics calculations.[32] Another study has shown that the nickel modification can improve the adsorption of water molecules on anatase-TiO_2, rutile-TiO_2, and ZnO photoanodes, enhancing their photoelectrochemical performance.[61] Particularly, Adsorption Locator for modelling has been broadly used for evaluating the adsorption interaction or non-bonded energies of organic and water molecules for various applications, including biomolecule/surface interactions,[62] adsorption of SiF_4 and HF gaseous molecules at the molecular level,[63] next-generation protein-based biosensor surfaces,[64] catalyst/adsorbents for oil recovery and viscosity reduction process,[65] drug delivery tool in biological systems,[66] *etc.* Here, the influence of the Al^{3+}–Mg^{2+} dual

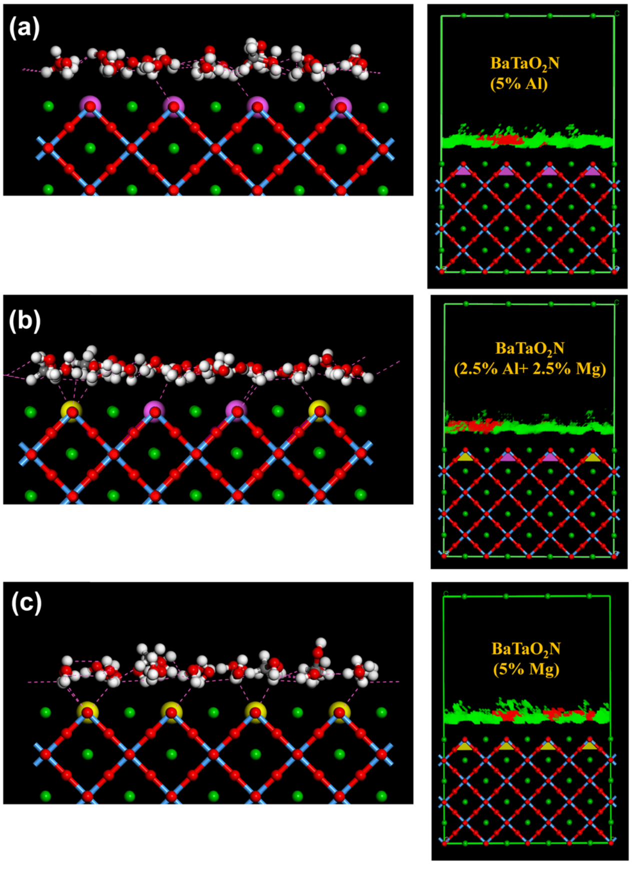

Fig. 7 Water and methanol molecules and field density distribution on the $BaTaO_2N(110)$ surfaces with 5% Al (a), 2.5% Al and 2.5% Mg (b), and 5% Mg (c). Atoms: grey – hydrogen, red – oxygen, blue – nitrogen, yellow – magnesium, pink – aluminum, light blue – tantalum, green – barium; *Isosurface*: red – methanol, green – water.

substitution on the adsorption of water molecules on the $BaTaO_2N(110)$ surfaces was also explored by combined Molecular Dynamics and Monte-Carlo computer simulation. The Forcite and Adsorption Locator modules in BIOVIA Materials Studio 2017 software[67] was used to determine the most favorable adsorption sites and to evaluate the adsorption energy of water molecules on the $BaTaO_2N(110)$ surfaces at different concentrations of the Al^{3+} and Mg^{2+} (co)substituents (Table S5, ESI†). The simulation data reveal that the adsorption energies of water molecules increase linearly by the Al^{3+}-for-Ta^{5+} substitution on the $BaTaO_2N(110)$ surface. The simultaneous adsorption of water and methanol molecules is higher than the adsorption of only water molecules (Fig. S4, ESI†), which increases depending on the Al^{3+} content. The differential adsorption (dE_{ads}/dN_i) of water molecules in water or water-methanol systems on the $BaTaO_2N(110)$ surfaces have similar values (2.3–2.7 kcal mol^{-1}). The methanol molecules interact more strongly with Al^{3+}–Mg^{2+}-cosubstituted surfaces (4.95–6.14 kcal mol^{-1}). Fig. 7 shows close contacts between water molecules and Al^{3+}–, Mg^{2+}– and Al^{3+}–Mg^{2+}-(co)substituted $BaTaO_2N(110)$ surfaces. However, methanol molecules tend to interact better with magnesium atoms on the $BaTaO_2N(110)$ surface. Thus, compared with Al^{3+}– or Mg^{2+} substitution, the Al^{3+}–Mg^{2+} dual substitution can improve the adsorption of water and methanol molecules on the surface of $BaTaO_2N$, enhancing its photocatalytic activity.

4. Conclusions

In summary, the partial Al^{3+}–Mg^{2+} dual substitution (5%) was applied to engineer structural defects and to modulate opto-electronic, surface, and photocatalytic activity of $BaTaO_2N$. The optical absorption edge of $BaTaO_2N$ was shifted to shorter wavelengths after (co)substitution of Al^{3+} and/or Mg^{2+} for Ta^{5+}, leading to the increase in the optical bandgap energy. This effect was more pronounced in the samples with higher content of Mg^{2+} because a large number of O^{2-} were substituted for N^{3-} to compensate charge balance. Similarly, a partial substitution of Mg^{2+} for Ta^{5+} affected the morphology of $BaTaO_2N$ particles in comparison to Al^{3+}, reducing the average particle size significantly. The initial reaction rates for the evolution of O_2 and H_2 revealed the improvement in the photocatalytic performance of $BaTaO_2N$ photocatalysts due to Al^{3+}–Mg^{2+} dual substitution. Particularly, $BaTaO_2N$ modified with 1.48% Al + 3.51% Mg generated the highest quantity of O_2 (178.66 μmol h^{-1}) and exhibited an apparent quantum yield of 0.18% at 420 nm, while $BaTaO_2N$ modified with 3.47% Al + 1.52% Mg produced the highest quantity of H_2 (18.94 μmol h^{-1}) and exhibited an apparent quantum yield of 0.64% at 420 nm. This enhancement in the photocatalytic O_2 and H_2 evolution over Al^{3+}–Mg^{2+}-(co)substituted $BaTaO_2N$ photocatalysts can be related to the changes in the defect density, dynamics of charge carriers, electronic band structure, improvement in water and methanol adsorption, and favorable shift in the band energy levels with respect to water reduction and oxidation potentials.

Conflicts of interest

There are no conflicts to declare.

Acknowledgements

The authors would like to thank Dr Ina Remy-Speckmann, Dipl. Phys. Christoph Fahrenson, Ms Reiko Shiozawa, and Dr Aleksei G. Krasnov for their kind assistance in XRD, SEM-EDX and XPS analyses and DFT calculations, respectively. This project received funding from the European Union's Horizon 2020 Research and Innovation Programme under the Marie Sklodowska-Curie grant agreement no. 793882.

References

1 Q. Wang and K. Domen, Particulate Photocatalysts for Light-Driven Water Splitting: Mechanisms, Challenges, and Design Strategies, *Chem. Rev.*, 2020, **120**, 919–985.

2 T. Takata and K. Domen, Defect engineering of photocatalysts by doping of aliovalent metal cations for efficient water splitting, *J. Phys. Chem. C*, 2009, **113**, 19386–19388.

3 W. J. Jo, H. J. Kang, K.-J. Kong, Y. S. Lee, H. Park, Y. Lee, T. Buonassisi, K. K. Gleason and J. S. Lee, Phase transition-induced band edge engineering of $BiVO_4$ to split pure water under visible light, *Proc. Natl. Acad. Sci. U. S. A.*, 2015, **112**, 13774–13778.

4 M. Tayebi and B.-K. Lee, The effects of W/Mo-*co*-doped $BiVO_4$ photoanodes for improving photoelectrochemical water splitting performance, *Catal. Today*, 2021, **361**, 183–190.

5 J. Xiao, B. Du, S. Hu, J. Zhong, X. Chen, Y. Zhang, D. Cai, S.-F. Zhou and G. Zhan, Simultaneously Enhanced Charge Separation and Transfer in Cocatalyst-Free Hematite Photoanode by Mo/Sn Codoping, *ACS Appl. Energy Mater.*, 2021, **4**, 10368–10379.

6 T. J. Smart, V. U. Baltazar, M. Chen, B. Yao, K. Mayford, F. Bridges, Y. Li and Y. Ping, Doping Bottleneck in Hematite: Multipole Clustering by Small Polarons, *Chem. Mater.*, 2021, **33**, 4390–4398.

7 Q. Wang, T. Hisatomi, S. S. K. Ma, Y. Li and K. Domen, Core/Shell Structured La- and Rh-Codoped $SrTiO_3$ as a Hydrogen Evolution Photocatalyst in Z-Scheme Overall Water Splitting under Visible Light Irradiation, *Chem. Mater.*, 2014, **26**, 4144–4150.

8 Y. Qin, F. Fang, Z. Xie, H. Lin, K. Zhang, X. Yu and K. Chang, La,Al-Codoped $SrTiO_3$ as a Photocatalyst in Overall Water Splitting: Significant Surface Engineering Effects on Defect Engineering, *ACS Catal.*, 2021, **11**, 11429–11439.

9 X. Sun, Y. Mi, F. Jiao and X. Xu, Activating Layered Perovskite Compound Sr_2TiO_4 via La/N Codoping for Visible Light Photocatalytic Water Splitting, *ACS Catal.*, 2018, **8**, 3209–3221.

10 A. Iwase, K. Saito and A. Kudo, Sensitization of $NaMO_3$ (M: Nb and Ta) Photocatalysts with Wide Band Gaps to Visible Light by Ir Doping, *Bull. Chem. Soc. Jpn.*, 2009, **82**, 514–518.

11 A. Iwase and A. Kudo, Development of Ir and La-codoped $BaTa_2O_6$ photocatalysts using visible light up to 640 nm as an H_2-evolving photocatalyst for Z-schematic water splitting, *Chem. Commun.*, 2017, **53**, 6156–6159.
12 A. Iwase and H. Misono, Development of visible-light-responsive Ir and La-codoped $KTaO_3$ photocatalysts for water splitting, *Chem. Commun.*, 2021, **57**, 10331–10334.
13 J. Seo, T. Takata, M. Nakabayashi, T. Hisatomi, N. Shibata, T. Minegishi and K. Domen, Mg–Zr Cosubstituted Ta_3N_5 Photoanode for Lower-Onset-Potential Solar-Driven Photoelectrochemical Water Splitting, *J. Am. Chem. Soc.*, 2015, **137**, 12780–12783.
14 J. Xiao, J. J. M. Vequizo, T. Hisatomi, J. Rabeah, M. Nakabayashi, Z. Wang, Q. Xiao, H. Li, Z. Pan, M. Krause, N. Yin, G. Smith, N. Shibata, A. Brückner, A. Yamakata, T. Takata and K. Domen, Simultaneously Tuning the Defects and Surface Properties of Ta_3N_5 Nanoparticles by Mg–Zr Codoping for Significantly Accelerated Photocatalytic H_2 Evolution, *J. Am. Chem. Soc.*, 2021, **143**, 10059–10064.
15 M. Higashi, R. Abe, K. Teramura, T. Takata, B. Ohtani and K. Domen, Two step water splitting into H_2 and O_2 under visible light by $ATaO_2N$ (A = Ca, Sr, Ba) and WO_3 with IO_3^-/I^- shuttle redox mediator, *Chem. Phys. Lett.*, 2008, **452**, 120–123.
16 K. Maeda and K. Domen, Water Oxidation Using a Particulate $BaZrO_3$-$BaTaO_2N$ Solid-Solution Photocatalyst That Operates under a Wide Range of Visible Light, *Angew. Chem., Int. Ed.*, 2012, **51**, 9865–9869.
17 S. Wei, G. Zhang and X. Xu, Activating $BaTaO_2N$ by Ca modifications and cobalt oxide for visible light photocatalytic water oxidation reactions, *Appl. Catal., B*, 2018, **237**, 373–381.
18 Z. Wang, Y. Luo, T. Hisatomi, J. J. M. Vequizo, S. Suzuki, S. Chen, M. Nakabayashi, L. Lin, Z. Pan, N. Kariya, A. Yamakata, N. Shibata, T. Takata, K. Teshima and K. Domen, Sequential cocatalyst decoration on $BaTaO_2N$ towards highly-active Z-scheme water splitting, *Nat. Commun.*, 2021, **12**, 1005.
19 S. Jadhav, S. Hasegawa, T. Hisatomi, Z. Wang, J. Seo, T. Higashi, M. Katayama, T. Minegishi, T. Takata, J. M. Peralta-Hernández, O. S. Torres and K. Domen, Efficient photocatalytic oxygen evolution using $BaTaO_2N$ obtained from nitridation of perovskite-type oxide, *J. Mater. Chem. A*, 2020, **8**, 1127–1130.
20 J. Seo, M. Nakabayashi, T. Hisatomi, N. Shibata, T. Minegishi and K. Domen, Solar-Driven Water Splitting over a $BaTaO_2N$ Photoanode Enhanced by Annealing in Argon, *ACS Appl. Energy Mater.*, 2019, **2**, 5777–5784.
21 M. Hojamberdiev, K. Yubuta, J. J. M. Vequizo, A. Yamakata, S. Oishi, K. Domen and K. Teshima, NH_3-Assisted Flux Growth of Cube-like $BaTaO_2N$ Submicron Crystals in a Completely Ionized Nonaqueous High-Temperature Solution and Their Water Splitting Activity, *Cryst. Growth Des.*, 2015, **15**, 4663–4671.
22 M. Hojamberdiev, K. Kawashima, T. Hisatomi, M. Katayama, M. Hasegawa, K. Domen and K. Teshima, Distinguishing the effects of altered morphology and size on the visible light-induced water oxidation activity and photoelectrochemical performance of $BaTaO_2N$ crystal structures, *Faraday Discuss.*, 2019, **215**, 227–241.
23 M. Hojamberdiev, J. M. Mora-Hernandez, R. Vargas, A. Yamakata, K. Yubuta, E. M. Heppke, L. M. Torres-Martínez, K. Teshima and M. Lerch, Time-Retrenched Synthesis of $BaTaO_2N$ by Localizing an NH_3 Delivery System for Visible-Light-Driven Photoelectrochemical Water Oxidation at Neutral pH: Solid-State Reaction or Flux Method?, *ACS Appl. Energy Mater.*, 2021, **4**, 9315–9327.
24 K. Teshima, Y. Hara, K. Yubuta, S. Oishi, K. Domen and M. Hojamberdiev, Application of Flux Method to the Fabrication of $Ba_5Ta_4O_{15}$, $Sr_5Ta_4O_{15}$, $Sr_2Ta_2O_7$, and $BaTaO_2N$ Polycrystalline Films on Ta Substrates, *Cryst. Growth Des.*, 2017, **17**, 1583–1588.
25 Y. Luo, Z. Wang, T. Yamada, K. Yubuta, S. Suzuki, T. Hisatomi, K. Domen and K. Teshima, Platy $BaTaO_2N$ Crystals Fabricated from K_2CO_3–KCl Binary Flux for Photocatalytic H_2 Evolution, *ACS Appl. Energy Mater.*, 2020, **3**, 10669–10675.
26 Y. Luo, S. Suzuki, Z. Wang, K. Yubuta, J. J. M. Vequizo, A. Yamakata, H. Shiiba, T. Hisatomi, K. Domen and K. Teshima, Construction of Spatial Charge Separation Facets on $BaTaO_2N$ Crystals by Flux Growth Approach for Visible-Light-Driven H_2 Production, *ACS Appl. Mater. Interfaces*, 2019, **11**, 22264–22271.
27 K. Hibino, M. Yashima, T. Oshima, K. Fujii and K. Maeda, Structures, electron density and characterization of novel photocatalysts, $(BaTaO_2N)_{1-x}(SrWO_2N)_x$ solid solutions, *Dalton Trans.*, 2017, **46**, 14947–14956.
28 Z. Lan, T. Vegge and I. E. Castelli, Theoretical Insight on Anion Ordering, Strain, and Doping Engineering of the Oxygen Evolution Reaction in $BaTaO_2N$, *Chem. Mater.*, 2021, **33**, 3297–3303.
29 K. Ueda, T. Minegishi, J. Clune, M. Nakabayashi, T. Hisatomi, H. Nishiyama, M. Katayama, N. Shibata, J. Kubota, T. Yamada and K. Domen, Photoelectrochemical Oxidation of Water Using $BaTaO_2N$ Photoanodes Prepared by Particle Transfer Method, *J. Am. Chem. Soc.*, 2015, **137**, 2227–2230.
30 T. Takata and K. Domen, Defect Engineering of Photocatalysts by Doping of Aliovalent Metal Cations for Efficient Water Splitting, *J. Phys. Chem. C*, 2009, **113**, 19386–19388.
31 M. Higashi, Y. Yamanaka, O. Tomita and R. Abe, Fabrication of Cation-Doped $BaTaO_2N$ Photoanodes for Efficient Photoelectrochemical Water Splitting Under Visible Light Irradiation, *APL Mater.*, 2015, **3**, 104418.
32 M. Hojamberdiev, R. Vargas, Z. C. Kadirova, K. Kato, H. Sena, A. G. Krasnov, A. Yamakata, K. Teshima and M. Lerch, Unfolding the Role of *B* Site-Selective Doping of Aliovalent Cations on Enhancing Sacrificial Visible Light-Induced Photocatalytic H_2 and O_2 Evolution over $BaTaO_2N$, *ACS Catal.*, 2022, **12**, 1403–1414.
33 Y. Bao, H. Zou, N. Yang, G. Li and F. Zhang, Synthesis of perovskite $BaTaO_2N$ with low defect by Zn doping for boosted photocatalytic water reduction, *J. Energy Chem.*, 2021, **63**, 358–363.

34 H. Zhang, S. Wei and X. Xu, Mg modified $BaTaO_2N$ as an efficient visible-light-active photocatalyst for water oxidation, *J. Catal.*, 2020, **383**, 135–143.

35 K. Maeda, D. Lu and K. Domen, Oxidation of Water under Visible-Light Irradiation over Modified $BaTaO_2N$ Photocatalysts Promoted by Tungsten Species, *Angew. Chem., Int. Ed.*, 2013, **52**, 6488–6491.

36 G. Kresse and J. Furthmüller, Efficient iterative schemes for ab initio total-energy calculations using a plane-wave basis set, *Phys. Rev. B: Condens. Matter Mater. Phys.*, 1996, **54**, 11169–11186.

37 D. Joubert, From ultrasoft pseudopotentials to the projector augmented-wave method, *Phys. Rev. B: Condens. Matter Mater. Phys.*, 1999, **59**, 1758–1775.

38 F. Pors, R. Marchand, Y. Laurent, P. Bacher and G. Roult, Etude structurale des perovskites oxyazotees $BaTaO_2N$ et $BaNbO_2N$. Structural study of $BaTaO_2N$ and $BaNbO_2N$ oxynitrided perovskites, *Mater. Res. Bull.*, 1988, **23**, 1447–1450.

39 J. P. Perdew, K. Burke and M. Ernzerhof, Generalized gradient approximation made simple, *Phys. Rev. Lett.*, 1996, **77**, 3865–3868.

40 J. E. Moussa, P. A. Schultz and J. R. Chelikowsky, Analysis of the Heyd-Scuseria-Ernzerhof density functional parameter space, *J. Chem. Phys.*, 2012, **136**, 1–11.

41 A. M. Ganose, A. J. Jackson and D. O. Scanlon, Sumo: Command-Line Tools for Plotting and Analysis of Periodic Ab Initio Calculations, *J. Open Source Softw.*, 2018, **3**, 717.

42 M. Hojamberdiev, E. Zahedi, E. Nurlaela, K. Kawashima, K. Yubuta, M. Nakayama, H. Wagata, T. Minegishi, K. Domen and K. Teshima, The Cross-Substitution Effect of Tantalum on the Visible-Light-Driven Water Oxidation Activity of $BaNbO_2N$ Crystals Grown Directly by an NH_3-Assisted Flux Method, *J. Mater. Chem. A*, 2016, **4**, 12807–12817.

43 Z. Ma, Z. Yi, J. Sun and K. Wu, Electronic and Photocatalytic Properties of $Ag_3PC_4^{VI}$ (C═O, S, Se): A Systemic Hybrid DFT Study, *J. Phys. Chem. C*, 2012, **116**, 25074–25080.

44 A. G. Krasnov, M. S. Napalkov, M. I. Vlasov, M. S. Koroleva, I. R. Shein and I. V. Piir, Photocatalytic Properties of $Bi_{2-x}Ti_2O_{7-1.5x}$ ($x = 0, 0.5$) Pyrochlores: Hybrid DFT Calculations and Experimental Study, *Inorg. Chem.*, 2020, **59**, 12385–12396.

45 M. A. Butler and D. S. Ginley, Prediction of Flatband Potentials at Semiconductor-Electrolyte Interfaces from Atomic Electronegativities, *J. Electrochem. Soc.*, 1978, **125**, 228–232.

46 M. Benčina, M. Valant and M. Ben, $Bi_2Ti_2O_7$-Based Pyrochlore Nanoparticles and Their Superior Photocatalytic Activity under Visible Light, *J. Am. Ceram. Soc.*, 2018, **101**, 82–90.

47 H. Sameie, A. A. Sabbagh Alvani, N. Naseri, S. Du and F. Rosei, First-Principles Study on ZnV_2O_6 and $Zn_2V_2O_7$: Two New Photoanode Candidates for Photoelectrochemical Water Oxidation, *Ceram. Int.*, 2018, **44**, 6607–6613.

48 K. Kawashima, M. Hojamberdiev, H. Wagata, M. Nakayama, K. Yubuta, S. Oishi, K. Domen and K. Teshima, Amount of tungsten dopant influencing the photocatalytic water oxidation activity of $LaTiO_2N$ crystals grown directly by an NH_3-assisted flux method, *Catal. Sci. Technol.*, 2016, **6**, 5389–5396.

49 K. Kawashima, M. Hojamberdiev, H. Wagata, K. Yubuta, K. Domen and K. Teshima, Protonated Oxide, Nitrided, and Reoxidized $K_2La_2Ti_3O_{10}$ Crystals: Visible-Light-Induced Photocatalytic Water Oxidation and Fabrication of Their Nanosheets, *ACS Sustainable Chem. Eng.*, 2017, **5**, 232–240.

50 Z. Xie, H. L. Tan, H. Wu, R. Amal, J. Scott and Y. H. Ng, Facet-dependent Spatial Charge Separation with Rational Co-catalyst Deposition on $BiVO_4$, *Mater. Today Energy*, 2022, **26**, 100986.

51 M. Zbiri, C. M. Aitchison, R. S. Sprick, A. I. Cooper and A. A. Y. Guilbert, Probing Dynamics of Water Mass Transfer in Organic Porous Photocatalyst Water-Splitting Materials by Neutron Spectroscopy, *Chem. Mater.*, 2021, **33**, 1363–1372.

52 M. Hojamberdiev and K. Kawashima, Exploring flux-grown transition metal oxynitride perovskites for photocatalytic water oxidation: A minireview, *Energy Rep.*, 2020, **6**, 13–24.

53 J. Seo, D. Ishizuka, T. Hisatomi, T. Takata and K. Domen, Effect of Mg^{2+} substitution on the photocatalytic water splitting activity of $LaMg_xNb_{1-x}O_{1+3x}N_{2-3x}$, *J. Mater. Chem. A*, 2021, **9**, 8655–8662.

54 C. Wang, T. Hisatomi, T. Minegishi, Q. Wang, M. Zhong, M. Katayama, J. Kubota and K. Domen, Synthesis of Nanostructured $BaTaO_2N$ Thin Films as Photoanodes for Solar Water Splitting, *J. Phys. Chem. C*, 2016, **120**, 15758–15764.

55 K. Kawashima, M. Hojamberdiev, K. Yubuta, K. Domen and K. Teshima, Synthesis and Visible-Light-Induced Sacrificial Photocatalytic Water Oxidation of Quinary Oxynitride $BaNb_{0.5}$-$Ta_{0.5}O_2N$ Crystals, *J. Energy Chem.*, 2018, **27**, 1415–1421.

56 X. Xu and H. Jiang, First-Principles Investigation on Anion Order, Electronic Structure and Dielectric Properties of $BaTaO_2N$, *J. Mater. Chem. A*, 2019, **7**, 14583–14591.

57 H. Kisch and D. Bahnemann, Best practice in photocatalysis: Comparing rates or apparent quantum yields, *J. Phys. Chem. Lett.*, 2015, **6**, 1907–1910.

58 F. Wu, G. Liu and X. Xu, Efficient photocatalytic oxygen production over Ca-modified $LaTiO_2N$, *J. Catal.*, 2017, **346**, 10–20.

59 C. Ni, C. Fu, B. Wang, H. Yuan and H. Chen, Charge-compensated codoped pseudohexagonal zinc selenide nanosheets towards enhanced visible-light-driven photocatalytic water splitting for hydrogen production, *Int. J. Hydrogen Energy*, 2021, **46**, 34305–34317.

60 A. Miyoshi, A. Kuwabara and K. Maeda, Effects of Nitrogen/Fluorine Codoping on Photocatalytic Rutile TiO_2 Crystal Studied by First-Principles Calculations, *Inorg. Chem.*, 2021, **60**, 2381–2389.

61 M. Hojamberdiev, R. Vargas, V. S. Bhati, D. Torres, Z. C. Kadirova and M. Kumar, Unraveling the photoelectrochemical behavior of Ni-modified ZnO and TiO_2 thin films fabricated by RF magnetron sputtering, *J. Electroanal. Chem.*, 2021, **882**, 115009.

62 S. Galvez-Martinez, E. Escamilla-Roa, M. P. Zorzano and E. Mateo-Marti, Defects on a pyrite (100) surface produce chemical evolution of glycine under inert conditions: experimental and theoretical approaches, *Phys. Chem. Chem. Phys.*, 2019, **21**, 24535–24542.

63 M. Khnifira, A. Mahsoune, M. E. Belghiti, L. Khamar, M. Sadiq, M. Abdennouri and N. Barka, HF and SiF_4 adsorption on carbon graphite (111) surface in aqueous medium: A combined DFT and MD simulation approach, *Mater. Today: Proc.*, 2021, **37**, 3987–3993.
64 J. S. Cross, Y. Kubota, A. Chatterjee, S. Unni, T. Ikoma and M. Tagaya, Interfacial Modeling of Fibrinogen Adsorption onto $LiNbO_3$ Single Crystal–Single Domain Surfaces, *Int. J. Mol. Sci.*, 2021, **22**, 5946.
65 T. Montoya, A. Amrollahi, G. Vitale, N. Hosseinpour and N. N. Nassar, Size Effects of NiO Nanoparticles on the Competitive Adsorption of Quinolin-65 and Violanthrone-79: Implications for Oil Upgrading and Recovery, *ACS Appl. Nano Mater.*, 2020, **3**, 5311–5326.
66 E. A. Abdullah, Theoretical study of a single-walled carbon nanotube and a cellulose biofiber as 5-fluorouracil *anti*-cancer drug carriers, *Eur. J. Chem.*, 2022, **13**, 69–77.
67 S. Sharma, P. Kumar and R. Chandra, Applications of BIOVIA Materials Studio, LAMMPS, and GROMACS in Various Fields of Science and Engineering, in *Molecular Dynamics Simulation of Nanocomposites Using BIOVIA Materials Studio, Lammps and Gromacs*, ed. S. Sharma, 2019, pp. 329–341.

